PCCP

PAPER

View Article Online
View Journal | View Issue

Cite this: *Phys. Chem. Chem. Phys.*, 2016, **18**, 14007

Understanding adsorption of CO_2, N_2, CH_4 and their mixtures in functionalized carbon nanopipe arrays†

Prosun Halder,‡ Manish Maurya,‡ Surendra K. Jain and Jayant K. Singh*

Received 2nd December 2015,
Accepted 13th April 2016

DOI: 10.1039/c5cp07422c

www.rsc.org/pccp

The selective adsorption behaviours of carbon dioxide, methane and nitrogen on bundles of functionalized CMK-5 are investigated at 303 K using grand-canonical Monte Carlo simulations. Functional groups (–OH, –COOH) cause a significant enhancement in CO_2 uptake (up to 19.5% at a pressure of 38.13 bar for –COOH). On the other hand, the adsorption amount of methane decreases with respect to bare CMK-5 by ~13% (at 38.13 bar) upon functionalization. Furthermore, functionalized CMK-5 with different pore sizes (4 nm, 6 nm, 8 nm) and inter-tube distances (d = 0 to 1.5 nm) are used to investigate the adsorption behaviour of flue gases. While the pore diameter is seen to reduce the isosteric heat of adsorption, the inter-tube distance of 0.25 nm shows the highest uptake of CO_2 at $p \leq 18$ bar, followed by 0.5 nm for the pressure range of $18 < p \leq 30$ bar, whereas for $p > 30$ bar, d = 1.0 nm shows the maximum uptake. For methane and nitrogen, the maximum adsorption is obtained at d = 0.25 nm in the studied pressure range. The selective adsorption of CO_2 in binary mixtures is investigated using ideal adsorption solution theory. CO_2–N_2 selectivity is found to increase significantly by surface functionalization of CMK-5 compared to pure CMK-5. The maximum selectivity of CO_2–CH_4 using –COOH functionalized CMK-5 is found to be ~10 for an equimolar CO_2–CH_4 mixture at a pressure of 38.13 bar.

1. Introduction

Nanoporous carbon-based materials have become the subject of major attention in recent years because of their potential applications as adsorbents, storage materials,[1,2] *etc.* These nanoporous carbon-based materials are of great interest because of their high stability, high surface activity,[3] low cost and weight. However, it is very challenging to control the pore morphology and topology of the classically used activated carbons during their preparation process.[4] Therefore, the materials do not possess well-ordered pores and uniform pore sizes. Some carbons, such as fullerenes and single-wall nanotubes (SWNTs), exhibit periodic structures[5,6] with voids that are potentially accessible to adsorbate molecules. The periodically arranged fullerenes and SWNTs are held together *via* weak van der Waals interactions[5,6] and thus can be considered as systems with permanent ordered porosity.[7] Recently, nanocasting using highly ordered mesoporous materials (such as silica) has made it possible to prepare novel mesostructured materials with permanent ordered porosity.[8] Ryoo *et al.* have shown that highly ordered mesoporous carbons can be obtained by templating highly ordered silica materials.[9] The template synthesis process to obtain mesoporous carbons is novel because it enables precise control of the porous structure of the final material. The structures of the carbons prepared in this way can be tailored by selecting the appropriate template material.[10] These carbon materials offer mechanical and thermal stability, high pore volume, electrical conductivity and useful surface properties. These materials are useful in various applications, which include separation of unwanted molecules from aqueous or gaseous phases,[11] catalysts in fuel cells and electrodes for capacitors.[12]

An important goal for the development of porous materials is the separation/removal of CO_2, which is emitted in industrial and environmental processes and is one of the main causes of global warming. While various studies[13–15] have been performed using the liquid–gas absorption based method for the separation of CO_2, the method has inherent disadvantages, such as low CO_2 loading, severe adsorbent corrosion and low contact area. On the other hand, the capture of CO_2 on mesoporous surfaces is much more effective, as summarized by Choi *et al.*[16] and Sayari *et al.*[17] in their excellent review on this topic. Plaza *et al.*[18] showed that activated carbon is a good adsorbent which is widely available and has high thermal stability. Although activated carbon has several favourable properties, its application is limited to high pressure gases.

Department of Chemical Engineering, Indian Institute of Technology Kanpur, Kanpur-208016, India. E-mail: jayantks@iitk.ac.in; Fax: +91 512 2590104; Tel: +91 512 2596141

† Electronic supplementary information (ESI) available. See DOI: 10.1039/c5cp07422c

‡ Prosun Halder and Manish Maurya contributed equally to this work.

Zeolite is also reported as an adsorbent; however, it is not efficient because of its large size, charge density and chemical composition, as shown by Wang *et al.*[19] Ordered mesoporous silica is a promising candidate because of its high surface area and highly ordered structure. Hence, several mesoporous silica materials (*e.g.* M41S, SBA-15, AMS) have been reported.[20–22] However, their adsorption isotherms are comparatively low. In the last decade, metal–organic frameworks (MOFs) have been intensively investigated.,[23–26] and have shown exceptional adsorption capacities at high pressure for MOFs. However, in the low pressure range, the adsorption isotherms for CO_2 show less adsorption. Additionally, several reports indicate low selectivity towards CO_2 from gas mixtures.[27,28] Recently, covalent organic frameworks (COF) were introduced as a new class of porous material. Unlike MOFs, COF structures are entirely composed of light elements (H, B, C, and O). Furukawa *et al.* have synthesized and used several COFs for clean energy applications; they found that COFs are among the best and most porous adsorbents for CO_2, CH_4, and H_2.[29] Earlier studies have shown that single-walled carbon nanotubes (SWCNT) can be used for adsorptive separation of CO_2.[30–33] Cinke *et al.*[30] found that the adsorption capacity was doubled for single-walled CNT compared to that of activated carbon. Hexagonally arranged multi walled carbon nanotubes (MWCNT) have also been used to investigate the adsorption behaviour of carbon dioxide.[34] Moreover, the surface chemistry of these materials can be tuned by adding functional groups or by altering the charge distribution of CNT to enhance the interaction.[35,36]

Recently, a variety of porous materials with regular pore structures have been developed to expand the realm of materials suitable for clean energy applications and to curtail the greenhouse effect. Among these, a porous material, CMK-5, displays some unique properties, including high surface area and large pore volume,[37,38] making it favourable as an adsorbent. CMK stands for carbon material of Korea because the first template based porous material was synthesized by Ryoo *et al.*[9] Since then, several CMK materials (up to CMK-9) have been synthesized using different templates and precursors during the synthesis.[39] Templated synthesis of ordered carbons can be performed *via* volume-templated or surface-templated carbons. In the first case, the entire void space of the template is infiltrated with carbon, whereas in the second case, carbon is introduced as a film on the pore surface of the template. The volume templating method gives a rod-like structure, while surface templating gives a pipe-like structure. A typical example of volume templating is CMK-3, in which carbon rods are arranged in a hexagonal symmetry. CMK-5 is the only surface templated carbon. Two techniques are widely used to enhance the adsorbate–adsorbent interaction: one is the fabrication of new porous material, and the other is surface functionalization, which creates new surface active sites. In this study, we have used molecular simulations to examine the effects of surface functionalization of CMK-5 on the adsorption behaviour of different flue gases.

2. Model and methodology

2.1. MCM-41 preparation

The MCM-41 pore was obtained by carving out a regular cylindrical pore of radius R_0 in an atomistic block of cristobalite (a non-porous silica mineral) following the method first introduced by Pellenq *et al.* to prepare a numerical sample of nanoporous silica materials.[40] To mimic the pore surface in a realistic way, the Si atoms, which are in an incomplete tetrahedral environment, were removed. All these steps were performed using in-house code. In the second step, all non-bonded oxygen atoms were removed. This procedure ensured that the remaining silicon atoms have no dangling bonds and the remaining oxygen atoms have at least one saturated bond with a Si atom. Subsequently, the electroneutrality of the simulation box was ensured by saturating all oxygen-dangling bonds with hydrogen atoms. The hydrogen atoms were placed in the pore void, perpendicularly to the pore surface, at a distance of 1 Å from the closest unsaturated oxygen atom. The structure was further relaxed by performing Monte Carlo simulations in the *NVT* ensemble using in-house code at a high temperature. More details regarding the MCM-41 pore model can be found in the work of Coasne *et al.*[41] The MCM-41 pore model used in our work has a pore diameter of 28 Å, 8398 atoms, and a pore length of 106.95 Å. A snapshot of the top and front view of the pore is shown in Fig. 1.

The above MCM-41 structure was used as a template for carbon adsorption. The interaction between the adsorbate (the carbon atoms) and the silica matrix was assumed to be weak and in the physisorption energy range. The interaction energy was calculated using the PN-TrAZ potential, a simplified version of the original PN-type potential function, as reported for the adsorption of rare gases and nitrogen in silicalite-1.[42]

The interaction between the carbon atoms was calculated using the Reactive Empirical Bond Order (REBO) potential proposed by Brenner.[43] The energy between two carbon atoms i and j was calculated using

$$U_{ij} = V_{ij}^{R}(r_{ij}) + b_{ij}V_{ij}^{A}(r_{ij}), \quad (1)$$

where V_{ij} is a pair repulsive term, V_{ij}^{A} is a pair attractive term and b_{ij} is a bond order term which weights the attractive part of the potential with respect to the repulsive part. The bond order term is a many body term which depends on the local environment of atoms i and j.

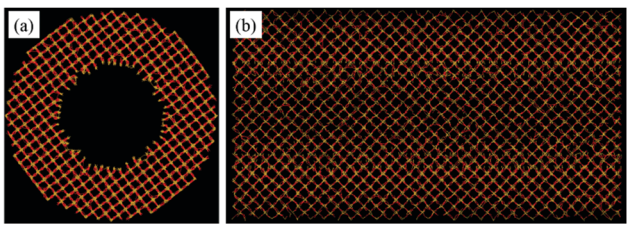

Fig. 1 The top view (a) and front view (b) of the MCM-41 pore.

Table 1 Interaction parameters of adsorbates and CMK-5 adsorbent[44,47,48]

Species	Site	σ (nm)	ε (kcal mol^{-1})	q (e)
CO_2	C	0.2757	0.0559	0.6512
	O	0.3033	0.16	−0.3256
N in (N_2)	N	3.31	0.072	−0.482
COM (in N_2)	N	0.0	0.0	0.964
CH_4	C	0.35	0.066	−0.24
	H	0.25	0.03	0.06
CMK-5	C	0.336	0.0556	0.0

2.2. Adsorption on CMK-5 surface

The intermolecular interaction energy between two molecules is expressed below:

$$E = 4\varepsilon_{ij}\left[\left(\frac{\sigma_{ij}}{r_{ij}}\right)^{12} - \left(\frac{\sigma_{ij}}{r_{ij}}\right)^{6}\right] + \frac{Cq_iq_j}{\varepsilon r_{ij}}. \quad (2)$$

The first term in the right hand side of eqn (2) represents the standard 12-6 Lennard-Jones potential, and the second term is the Columbic pairwise interactions between site i and site j of two different molecules.

The potential parameters for CMK-5 were taken from Peng *et al.* (2009).[44] N_2 was modeled by the TraPPE force field proposed by Potoff *et al.*,[45] whereas CH_4 was modeled using a four-site model.[46] The CH_4 potential parameters were taken from the OPLS model proposed by Jorgensen *et al.* (1990).[47] In the case of CO_2, the EPM2 model proposed by Harris and Yung[48] was used. All the molecules were considered to be rigid; hence, the bond bending potential was not included. The interaction parameters for different atoms are listed in Table 1. The Lennard-Jones interactions between unlike atoms were approximated using Lorentz–Berthelot rules.[49] Interaction between two molecules beyond 1 nm was neglected to reduce the computational time. The number of atoms was varied from 16 000 to 80 000.

2.3. Adsorption theory

The adsorption or surface excess of a given component is defined as the difference between the amount of component actually present in the system, and that which would be present (in a reference system) if the bulk concentrations in the adjoining phases were maintained up to a chosen geometrical dividing surface. Thus, the absolute adsorption amount was converted into excess adsorption of the adsorbate using eqn (3),

$$N_{ex} = N_{ad} - \rho_b V_{free}, \quad (3)$$

where N_{ex} and N_{ad} are the excess and absolute adsorption amounts, respectively. ρ_b is the bulk density of the adsorbate, and V_{free} is the accessible volume for gas particles. Bulk density can be calculated by performing independent grand-canonical Monte Carlo (GCMC) simulations at different chemical potentials. There are various methods to calculate the free volume.[50–52] In this work, the free volume was calculated using a helium (He) adsorption technique.[53]

The adsorptive characteristics of an adsorbent can also be analysed by studying the strength of the adsorbent–adsorbate interaction given by the heat of adsorption, which can be obtained from GCMC simulations. Isosteric heat of adsorption[54] (q_{st}) is usually expressed in the approximated form as:

$$q_{st} \approx RT - \left(\frac{\partial U_{ad}}{\partial N_{ad}}\right)_{T,V}, \quad (4)$$

where U_{ad} is the potential energy of the adsorbed phase. Eqn (4) can be further modified in the form given below:

$$q_{st} = RT - \frac{\langle U_{ad}N_{ad}\rangle - \langle U_{ad}\rangle\langle N_{ad}\rangle}{\langle N_{ad}{}^2\rangle - \langle N_{ad}\rangle^2}, \quad (5)$$

where the angled brackets represent an ensemble average.

Adsorption selectivity in a binary mixture of components i and j is defined as

$$S_{i/j} = \left(\frac{x_i}{x_j}\right)\left(\frac{y_i}{y_j}\right) \quad (6)$$

where x_i and y_i are the mole fractions of component i in the adsorbed and bulk phases, respectively.

3. Simulation details

3.1. CMK-5 preparation

We began with a MCM-41 cylindrical pore model as a template for our CMK-5 model. We subsequently performed GCMC simulations for the adsorption of carbon atoms in an MCM-41 pore model of diameter 28 Å and a length of 106.95 Å, as shown in Fig. 2a. In the usual experimental procedure for CMK-5 preparation, adsorption of a polymer inside the silica template is first performed. This is followed by carbonization (heating at high temperature) and removal of the silica template. We avoided following the exact experimental procedure, as our interest is in the final structure of the porous matrix. Thus, in this molecular simulation work, the carbon atoms are first adsorbed in the MCM-41 pore. This is achieved at a high temperature of 3000 K, as at lower temperatures the adsorption process of carbon atoms is not efficient due to the low acceptance ratio. The GCMC code for the development of the CMK-5 (using REBO potential for the interaction between carbon atoms and PNTraz potential for the interaction between silica and carbon atoms) was developed in the group of Keith Gubbins at NCSU. Periodic boundary conditions are assumed only along the pore axis (*X*-axis) to obtain the cylindrical pipe shape. In order to

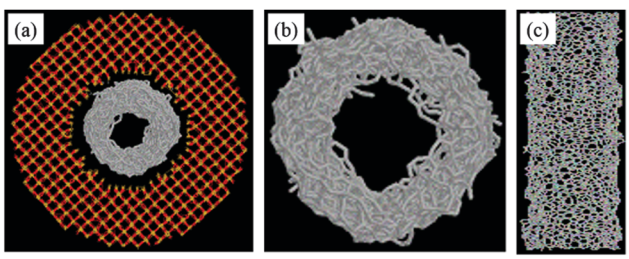

Fig. 2 (a) Carbon pipe obtained by carbon adsorption in the MCM-41 pore. Carbon pipe obtained after removing the silica template and relaxing the carbon structure: (b) top view and (c) side view.

increase the speed of the simulation, we divided the simulation box into a fine grid of 100 × 100 × 100 and calculated the interaction of one adsorbate (carbon) atom with the adsorbent (MCM-41 silica) at each grid point. During the GCMC simulation, the adsorbate–adsorbent potential energy was calculated using a trilinear interpolation in the energy grid. Starting with many carbon dimers located near the pore surface, we gradually raised the chemical potential and recorded the average number of adsorbed carbon atoms. We stopped the simulation when we reached the specified pore width of carbon atoms inside the MCM-41 pore, which decides the diameter of the CMK-5. We then removed the MCM-41 silica template and obtained the final carbon structures (pipes), which are roughly cylindrical. These carbon structures (individual carbon pipes) were then relaxed (relaxed in *NVT* ensemble) with REBO potential. The radial distribution function of the C–C atoms of this material can be found in the ESI† (S1). Since experimentally[37] obtained CMK-5 is hexagonally arranged, we placed the final relaxed individual amorphous carbon pipes in a hexagonal lattice using VMD (Visual Molecular Dynamics) software[55] to obtain CMK-5 models with different inter-tube distances. The inter-tube distance results were obtained assuming a periodic structure of CMK-5, although the basic structure is highly amorphous. CMK-5 is a carbon material that has carbon nanopipes arranged in hexagonal symmetry. Therefore, in this work, CMK-5 refers to all the models in which carbon pipes are arranged in hexagonal symmetry (irrespective of tube diameters and inter-tube distances).

The final CMK-5 structures are amorphous, as the carbon atoms are present in a disordered configuration. We emphasize that we are not mimicking the synthesis process in our simulations. In reality, a carbon precursor is infiltrated into the silica template and is then polymerized and carbonized to obtain the carbon. In our case, we are not simulating the polymerization or carbonization process, as we are interested in the final carbon structure only. By simulating the carbon adsorption in a silica pore, we obtain a carbon structure that resembles and contains the features of a realistic carbon replica obtained from a silica template.

The carbon–silica (fluid–wall) potential energy in our case is physisorption energy, and thus is much smaller in magnitude than the carbon–carbon (fluid–fluid) energy that involves the formation of a covalent bond. Thus, the wetting of the silica surface by carbon atoms, which is necessary to obtain carbon pipes, is not observed. Hence, we increased the fluid-wall potential energy at each grid point by multiplying the fluid-wall energy obtained with the PN-Traz potential[42] with a fixed integer. The use of the reactive REBO potential ensures that the chemistry of the carbon atoms is correctly reproduced at the local level. The final carbon structures (carbon nanopipes) consist of rings (5,6, and 7-membered) of carbon atoms, as found in microporous carbon models.[56,57] The final structure of CMK-5 is shown in Fig. 2b and c.

3.2. Functionalization

We added different functional groups to our arrays of carbon nanopipes to study the effects of functional groups on adsorption.

Table 2 Interaction parameters of functional groups[58]

Group	Site	σ (nm)	ε (kcal mol^{-1})	q (e)
Hydroxyl	C[a]			0.2
	O	0.307	0.1554	−0.64
	H			0.44
Carboxyl	C[a]			0.08
	C	0.375	0.1033	0.55
	O	0.296	0.21	−0.5
	O	0.3	0.1701	−0.58
	H			0.45

C[a] is the carbon located in the plane of the nanopipe surface.

The method to add functional groups is as follows: we randomly selected a carbon atom and added a functional group in the radial direction perpendicular to the pore wall. We then checked for overlap of the functional group with other carbon atoms of the matrix and with other functional groups that were already added. If an overlap existed, we did not add the functional group and we randomly selected another carbon atom to add the functional group.

The functional groups are attached to the internal surface as well as to the external surface of the carbon nanopipes. In this work, two different groups were used, namely carboxyl (–COOH) and hydroxyl (–OH) groups. The distance, angle and potential parameters are tabulated in Table 2. We varied the percentage of functionalization (by weight) from 2% to 5%.

3.3. Simulation setup

Fig. 3 shows the schematic of micro-porous nanopipes in a unit cell where the nanopipes are arranged in a hexagonal lattice. The simulation box is periodic in all three directions. Since the diameter of the tube is not constant, the external diameter was used for obtaining the cell dimensions. Different inter-tube distances, *viz.*, 0 nm, 0.25 nm, 0.5 nm, 1 nm, and 1.5 nm, were used to analyse the effects of porosity. In a unit cell, two nanopipes were placed to observe the adsorption on the internal nanopipe surface as well as on the external nanopipe surface. The length of the unit cell in the direction of the nanopipe axis was fixed at 8.14 nm. The remaining dimensions of the unit cell were adjusted using the external diameter of the nanopipe and the inter-tube distance. GCMC simulations were conducted to study the adsorption of various gas molecules. Carbon dioxide, methane and nitrogen were used as adsorbates for this adsorption simulation. The temperature and volume of the simulation box were kept constant. Multiple simulations were conducted using different chemical potential values to generate the adsorption isotherm. The pressure calculations can be found in the ESI† (S2). Since flue gas is generally cooled to 25 °C to 30 °C before the removal of CO_2, we fixed the temperature to 303 K for the current study. Three Monte Carlo (MC) moves were employed in the simulation. The probabilities for the different moves were 0.2 for the translation move, 0.1 for the rotational move, and 0.7 for the addition/deletion move. Each GCMC simulation consisted of an equilibration run of 2.5×10^7 MC steps and an equal amount of steps for the production run.

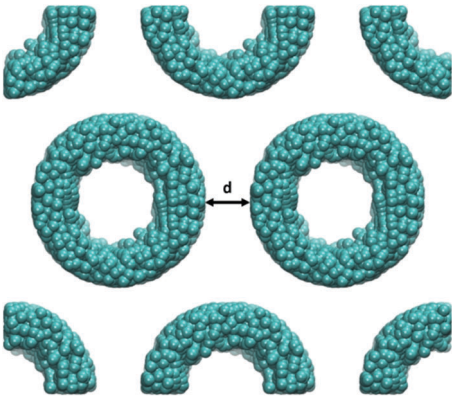

Fig. 3 Schematic of CMK-5 used in the GCMC simulations, with an inter-tube distance *d*.

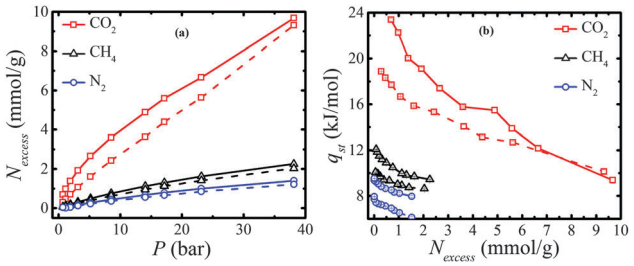

Fig. 6 (a) Excess adsorption of CO_2, CH_4, and N_2 as a function of pressure and (b) heat of adsorption as a function of excess adsorption in functionalized CMK-5 arrays with a pore diameter of 4 nm and an inter-tube distance of 1.0 nm at 303 K. Solid and dashed lines represent adsorptions in carboxyl group and hydroxyl group (4% by weight) functionalized CMK-5, respectively.

4. Results and discussion

4.1. Adsorption on pure CMK-5

We start the discussion with the adsorption isotherms of pure CO_2, CH_4 and N_2 on the bare CMK surface, as shown in Fig. 4.

The excess adsorption increases with pressure, as expected, for all three gases considered in this work, although the behavior is dependent on the type of the gas molecule. While CO_2 is more favorable as an adsorbate, reaching 7.8 mmol g^{-1} at P = 38.14 bar, the corresponding values for N_2 and CH_4 are $\sim$1.5 and 2.5 mmol g^{-1}, respectively. The amount of gas uptake is in the order of $N_2 < CH_4 < CO_2$, which is in accordance with the interaction strengths of the gases with CMK-5. To obtain a better understanding of the adsorption behavior, the local density is presented in Fig. 5. Two distinguishable peaks are observed next to the inside and outside of the pore wall for each case, indicating monolayer adsorption of gas molecules on the nanopipe wall. The pronounced adsorption with increasing pressure is evident from the increase in the peak height of the density profile with pressure. Furthermore, it is clear that adsorption, for $P \leq$ 23.13 bar, occurs within the first layer next to the CMK-5 surface. Nevertheless, the formation of a second layer is initiated at higher pressure. At lower pressures, the peak height inside the pore is greater than the peak height in the inter-tube region. However, at higher pressures, the peak heights are similar.

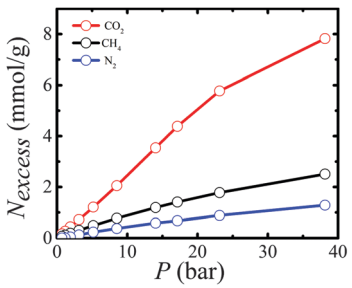

Fig. 4 Excess adsorption isotherms of CO_2, CH_4, and N_2 in bare CMK-5 arrays with a tube diameter of 4 nm and an inter-tube distance of 1 nm at T = 303 K.

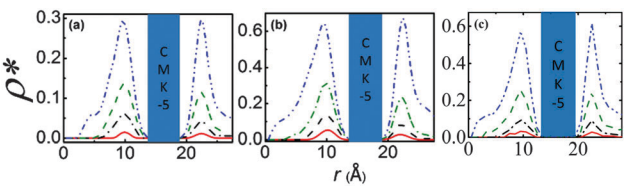

Fig. 5 Local density profiles of (a) CH_4, (b) CO_2, (c) N_2 adsorbed on the surface of the pore wall. Herein, r is the distance from the nanopipe center. The dash dot dotted, dashed, dash dotted, and straight lines represent the density profiles at 23.13, 8.51, 3.13, and 1.15 bar, respectively.

4.2. Adsorption on functionalized CMK-5

Fig. 6a presents the effects of carboxyl and hydroxyl functionalized CMK-5 on the adsorption isotherms of CO_2, CH_4 and N_2. For all gases, carboxylic group functionalized CMK-5 shows much greater affinity for adsorption than hydroxyl group functionalized CMK-5.

At higher pressures, for CO_2, the excess adsorption is comparatively higher for both carboxyl group functionalized CMK-5 and hydroxyl group functionalized CMK-5 than for pure CMK-5. At P = 38.14 bar, the excess adsorption isotherm of carbon dioxide is 9.7 mmol g^{-1} (for pure CMK-5, it is $\sim$8 mmol g^{-1}). However, in the case of methane, the excess adsorption isotherm at higher values of pressure is less than that seen for the bare CMK-5. The binding energy or effective interaction strength of gas molecules with CMK-5 can be interpreted from q_{st} when the number of gas molecules approaches zero (see eqn (4)). Hence, a higher q_{st} at a lower value of N_{excess} indicates a higher interaction strength of the gas molecule with the CMK-5. The corresponding values for nitrogen and CO_2 are $\sim$10 kJ mol^{-1} and $\sim$24 kJ mol^{-1}, respectively. This supports the observation of low amounts of adsorption for nitrogen. The effect of the functional group is also reflected in the heat of adsorption, as shown in Fig. 6b. In most cases, q_{st} monotonically decreases with increasing adsorption amount, which is expected (until the monolayer is saturated). In the case of carboxyl group functionalized CMK-5, the interaction strength is higher than that for hydroxyl group functionalized nanopipes for all adsorbates. For further investigation, snapshots of carbon dioxide, methane

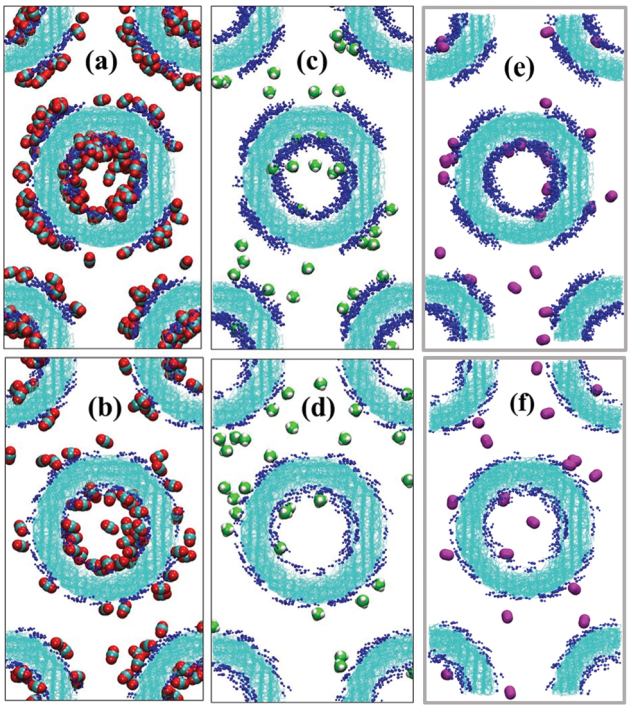

Fig. 7 Images of CO_2 (a and b), CH_4 (c and d), N_2 (e and f) in 4% –COOH (top) and –OH (bottom) functionalized CMK-5 arrays with 4 nm diameter and 1 nm inter-tube distance at 1.15 bar and 303 K. Blue color represents the functional groups attached to CMK-5.

and nitrogen in different functionalized CMK-5 are presented in Fig. 7.

The snapshots illustrate that at a given pressure, the adsorption amount for all the gases is higher for –COOH functionalized nanopipes than for –OH functionalized nanopipes. It is observed that –COOH functionalization allows the monolayer to be filled within the interior section of the pore, in contrast to the –OH functionalized CMK-5. The snapshot also reveals that CO_2 has the strongest interaction with functionalized CMK-5, as depicted by the enriched amount of adsorption within the pore. While the –OH group also causes significant adsorption, as observed by the appearance of a second layer in the case of CO_2, the effect is not as pronounced as that seen for –COOH. Afterward, the functionalization density of CO_2 slightly increases inside the CMK-5 compared to outside the CMK-5. This behavior is attributed mainly to the increased density of the functional groups within the pore, leading to preferential adsorption inside the pore. Hence, the density inside the pore increases with increasing pressure. This is also evident from the snapshots shown in Fig. 7.

4.3. Effect of different amounts of functionalization

Now, we turn our attention to the effect of different amounts of functionalization on the excess adsorption and heat of adsorption. Fig. 8 (top) presents the excess adsorption of CO_2, CH_4, and N_2 for different percentages of carboxylic group functionalized CMK-5. In the case of carbon dioxide, the excess adsorption increases with increasing amount of –COOH groups.

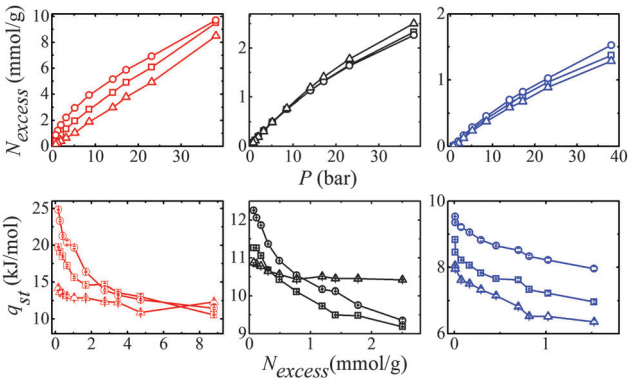

Fig. 8 Excess adsorption isotherm (top) and isosteric heat of adsorption (bottom) of CO_2 (red), CH_4 (black), and N_2 (blue) in –COOH group functionalized CMK-5 with 4 nm pore size and 1 nm inter-tube distance. The triangle, square, and circle symbols represent pure CMK-5, 2% –COOH functionalized CMK-5, and 5% –COOH functionalized CMK-5, respectively.

However, a relatively negligible enhancement of excess adsorption is seen for methane and nitrogen (particularly at low pressure). Since the interaction strengths of methane and nitrogen with both functional groups are weak, the increase in the percentage of functionalization does not cause significant enhancement in their adsorption amounts. However, the heat of adsorption for –COOH functional CMK-5 shows some significant changes, as seen in Fig. 8 (bottom). At a lower pressure, the electrostatic and dispersion interactions between the carbon dioxide molecules and –COOH groups play a major role in the significant enhancement of the heat of adsorption (at a lower value of excess adsorption), which is seen relatively less for CH_4 and N_2. This can be seen in the snapshot given in the ESI† (S3).

Fig. 9 presents the excess adsorption and heat of adsorption for CO_2, CH_4, and N_2 in hydroxyl functionalized CMK-5. For methane and nitrogen, a slight deviation in the adsorption isotherm from pure CMK-5 is seen with increasing amounts of functional groups, which is also supported by the isosteric heat of adsorption. This is attributed to the lesser attraction of

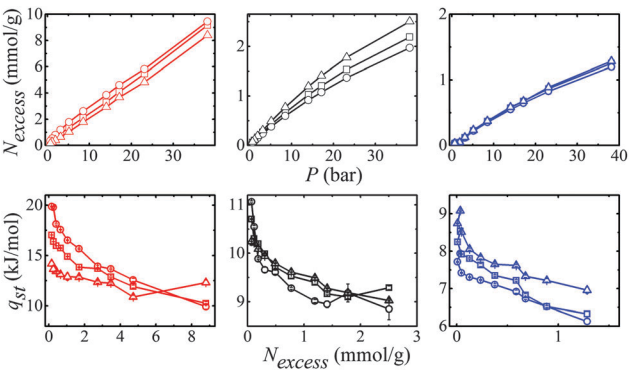

Fig. 9 Excess adsorption isotherm (top) and isosteric heat of adsorption (bottom) of CO_2 (red), CH_4 (black), and N_2 (blue) in –OH group functionalized CMK-5, with 4 nm pore diameter and 1 nm inter-tube distance. The triangle, square, and circle symbols represent pure CMK-5, 2% functionalized CMK-5, and 5% functionalized CMK-5, respectively.

methane and nitrogen towards the functional group. With increasing percentage functionalization, the active sites decrease for methane and nitrogen molecules, leading to a decrease in the adsorption amount. In the case of nitrogen, the effect is extremely small, and can be neglected for the given pressure range. Meanwhile, for CO_2, the excess adsorption increases slightly with the introduction of additional –OH functional groups due to the stronger interaction strength of CO_2 with the functional groups, unlike that for methane and nitrogen.

In comparison with the adsorption amount for the gas molecules in pure CMK-5, the adsorption amount for CO_2 was found to increase significantly with the introduction of more carboxyl groups. For example, 5 wt% functionalized CMK-5 with –COOH groups enhances the amount of adsorption of CO_2 by 19.5%. On the other hand, for methane, the situation is quite the opposite for –OH functionalized CMK-5, *i.e.* the presence of more functional groups leads to a decrease in the adsorption amount such that for 5 wt% –OH functionalized CMK-5, a ~13% reduction in the excess adsorption is seen compared to bare CMK-5. The CO_2 capacities of functionalized CMK-5 with –COOH and –OH groups reac 9.7 and 9.4 mmol g^{-1} at ~38 bar and 303 K, respectively, which is close to the experimental CO_2 uptake of CMK-3 (10.5 mmol g^{-1} at 298 K) using similar hexagonal arrangements.[59] However, our results differ from those of Peng *et al.*,[60] who obtained a CO_2 capacity of 28 mmol g^{-1} at 40 bar and 298 K on bare CMK-5; this is significantly higher than the corresponding value in our case (8.5 mmol g^{-1} at 38 bar and 303 K in bare CMK-5). It should be noted that the models used in this work and by Peng *et al.* are dramatically different. While we have considered an all atom approach, Peng *et al.* considered a non-structured surface for CMK-5 and single site beads for fluid molecules. We believe that the difference in the models may be reason for the discrepancy.

4.4. Effect of pore diameter

Since adsorption behavior depends on the structure and geometrical size of a material, we have studied the effect of the pore size of CMK-5 on the separation and storage of flue gases. Here, we used three different pore sizes, *viz.*, 4 nm, 6 nm and 8 nm. We show that for any operating storage pressure, there is a unique nanopipe size that maximizes the overall gravimetric uptake of a flue gas. The excess adsorption isotherms for the 2% carboxylic group functionalized CMK-5 with different diameters and a constant inter-tube distance of 1.0 nm are given in Fig. 10.

It is evident from Fig. 10 that as the pore diameter is increased, the excess adsorption decreases though absolute adsorption would still increase,[61,62] as can be seen in Fig. 11. The uptake of each pure gas decreases with increasing diameter due to the increase in the curvature of CMK-5. This in turn resulted in a decrease in the local density of adsorbate molecules around the adsorbent molecule because of the reduced interaction with the adsorbate. As the pore diameter increases from 4 nm to 6 nm, a significant decrease in the excess adsorption is seen. However, the decrease in the excess adsorption is slight

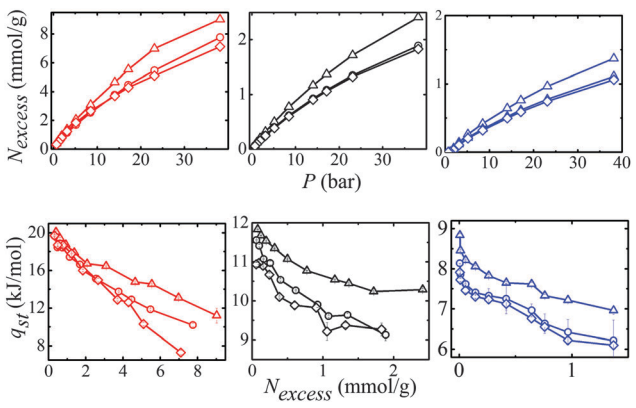

Fig. 10 Excess adsorption isotherm (top) and isosteric heat of adsorption (bottom) of carbon dioxide (red), methane (black) and nitrogen (blue) in 2% carboxylic group functionalized CMK-5, with 1 nm inter-tube distance, at 303 K, respectively. Symbols, triangle, circle, and diamond represent 4 nm, 6 nm, and 8 nm diameter, respectively.

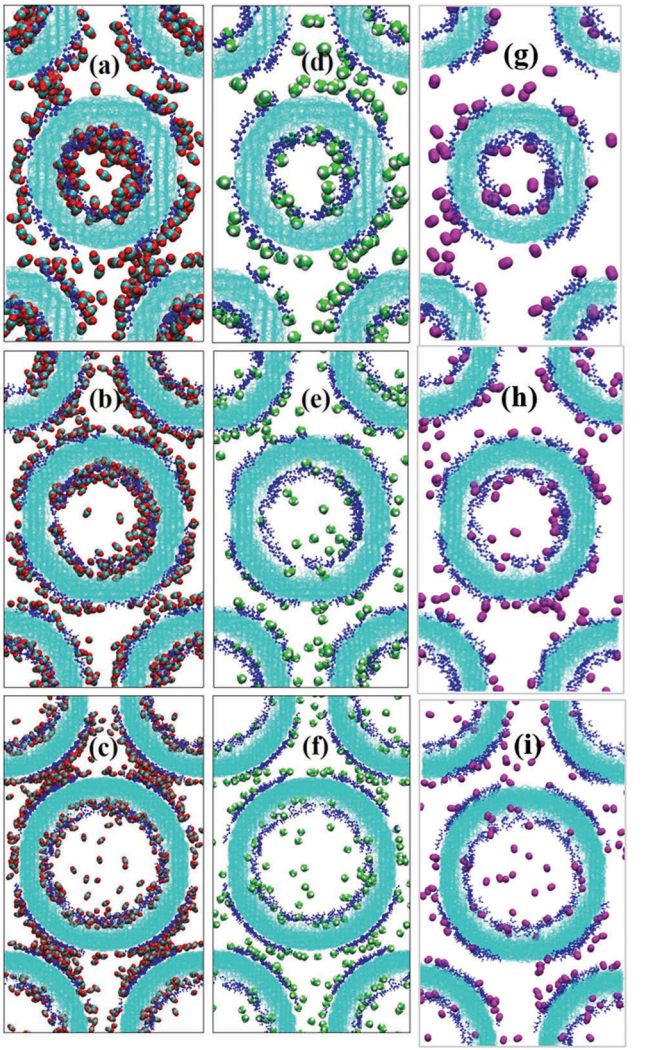

Fig. 11 Images of absolute loading of CO_2 (a–c), CH_4 (d–f), and N_2 (g–i) in 2% functionalized CMK-5 with diameters of 4, 6, and 8 nm, respectively at 3.13 bar, 303 K. Blue color represents the functional groups attached to CMK-5.

when the diameter increases from 6 nm to 8 nm. Similar behavior has been observed in earlier studies.[63] The effect of diameter was also noted on the isosteric heat of adsorption, as shown in Fig. 10 (bottom). We observe that the isosteric heat of adsorption decreases with increasing pore width. This phenomenon can be explained in terms of the fluid–fluid interactions and the fluid–solid molecule interactions. Fluid–fluid interaction dominates at high loading because of the greater number of neighboring adsorbed molecules. Meanwhile, solid–fluid interactions dominate at low loading because of the overlapping of solid–fluid potential from both neighboring and opposite solid pore molecules. At higher pore widths, the contribution from the opposite pore wall decreases, and hence the total isosteric heat of adsorption decreases with pore width. Similar observations were made by Peng *et al.*[64] q_{st} typically decreases with excess adsorption until the monolayer is saturated (or before the initiation of second or higher layers). The effect of diameter is not seen to be great at lower pressures or lower values of adsorption on q_{st}.

4.5. Effect of inter-tube distance on adsorption

Fig. 12 shows the adsorption isotherms of CO_2, CH_4 and N_2 for different inter-tube distances (d = 0 to 1.5 nm) on bare CMK-5. At a lower inter-tube distance, the isotherm saturates at lower values of pressure. This is mainly due to the lower volume available for adsorption. However, with increasing inter-tube distance, the saturation occurs at higher pressures. This is evident for the case of CO_2 within the pressure range studied in this work. The inter-tube distance affects the excess adsorption by affecting the groove regions. At lower inter-tube distance, the grooves are the preferred adsorption regions, which is not the case for higher inter-tube distances, leading to crossover behavior of the adsorption isotherm. The inter-tube distance of 0.25 nm shows the highest uptake of CO_2 up to pressures $\leq$18 bar, followed by the 0.5 nm inter-tube distance for the pressure range of 18 $< p \leq$ 30 bar. For all other pressures $\geq$30 bar, the maximum uptake of CO_2 is observed at d = 1.0 nm. For methane and nitrogen, the maximum adsorption is observed at d = 0.25 nm in the studied pressure range.

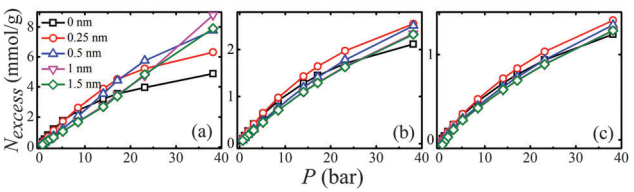

Fig. 12 Effect of different inter-tube distances of bare CMK-5 on the adsorption capacity of (a) CO_2, (b) CH_4, and (c) N_2.

For methane and nitrogen gases, the maximum uptake is observed at d = 0.25 nm due to enhanced adsorption in the groove regions. However, with further increase in the inter-tube distance, the amount of adsorption decreases due to the weak affinity of methane and nitrogen gases with CMK-5 carbon atoms. Nevertheless, the effect of inter-tube distance is relatively less for CH_4 and N_2 compared to that seen for CO_2.

4.6. Fitting of adsorption isotherms from GCMC simulations

In order to predict the adsorption isotherms of binary mixtures, we first fit the adsorption isotherms of pure components using the Langmuir isotherm equation. The model parameters obtained from the fit for different adsorbates in functionalized CMK-5s are tabulated in Table 3. In order to predict the adsorption behavior of binary gas mixtures, we used IAST, which utilizes the absolute adsorption isotherms of the pure components. In this work, we estimated the adsorption isotherms of 3 types

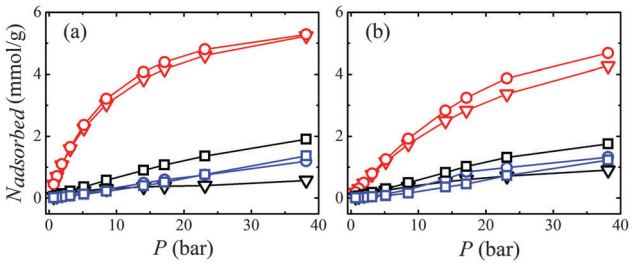

Fig. 13 Adsorption isotherms of equimolar mixtures by IAST prediction in 5% (a) –COOH, (b) –OH functionalized CMK-5 with a diameter of 4 nm and an inter-tube distance of 1.5 nm. The triangle, circle, and square symbols represent CO_2/CH_4, CO_2/N_2 and CH_4/N_2 mixtures, respectively. The colors red, black and blue represent CO_2, CH_4 and N_2, respectively.

Table 3 Model parameters for the Langmuir isotherm equation obtained by fitting absolute adsorption isotherms from GCMC simulations. q is the monolayer capacity (mmol g^{-1}) and k is the Langmuir constant (bar^{-1})

				CMK-5 functionalization			
				–OH		–COOH	
Component	Pore diameter (nm)	% Functionalization	Inter-tube distance (nm)	q	k	q	k
CO_2	4	2	0.5	25.071	0.015	9.66	0.063
	6	4	1.0	9.192	0.042	7.22	0.135
	8	5	1.5	9.139	0.047	6.26	0.233
CH_4	4	2	0.5	8.494	0.014	6.76	0.02
	6	4	1.0	8.748	0.011	5.94	0.021
	8	5	1.5	10.122	0.01	6.13	0.022
N_2	4	2	0.5	0.97	0.03	1.98	0.019
	6	4	1.0	0.253	0.05	1.15	0.026
	8	5	1.5	0.085	0.07	1.01	0.03

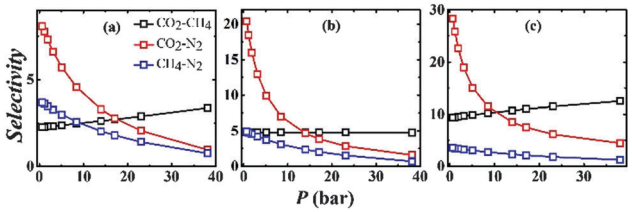

Fig. 14 Selectivity of equimolar mixtures by IAST prediction in bare CMK-5 (a) and 5% (b) –OH, (c) –COOH functionalized CMK-5 with a diameter of 4 nm and an inter-tube distance of 1 nm.

of equimolar binary mixtures, *viz.* CO_2–CH_4, CH_4–N_2, and CO_2–N_2.

Fig. 13 presents the total adsorption amounts of different binary gas mixtures in the functionalized CMK-5. The trends observed for the adsorption isotherms of different gases in the mixtures are similar to those observed for the pure component isotherms. The CO_2 adsorption capacity is the highest for COOH functionalization. Adsorption uptake can be analyzed by the Langmuir's constants listed in Table 3. The values of the Langmuir's constants correlate well with the maximum monolayer capacities of the OH and COOH functionalized CMK-5.

Furthermore, we also observed that the adsorption rate is high for COOH functionalization compared to OH functionalization, as the COOH modified surface saturates more quickly. The IAST data is used to examine the selectivity of different functionalized CMK-5, which is shown in Fig. 14.

It is observed that –COOH functionalized CMK-5 is more selective towards carbon dioxide than the other gases. The selectivity for the mixtures studied in this work follows the order $S_{CH_4\text{–}N_2} < S_{CO_2\text{–}CH_4} < S_{CO_2\text{–}N_2}$. For the CH_4–N_2 binary mixtures, the selectivity varies in the range of 2 to 5 and increases slightly upon functionalization.

In the case of the CO_2–CH_4 mixture in –COOH functionalized CMK-5, the selectivity towards CO_2–CH_4 is $\sim$10 at $P \sim 38$ bar, which is around 2 times higher than that of the bare CMK-5. The selectivity increases significantly for the CO_2–N_2 mixture after functionalization of CMK-5 with –OH and –COOH groups. The current study suggests that while the CO_2 adsorption capacity of CMK-5 is not enhanced dramatically, the selectively is significantly higher (200%) for –COOH functionalized CMK-5. This is primarily due to the effect of –COOH, which leads to an enhancement of CO_2 adsorption along with a decrease in the adsorption capacity of other gases, leading to higher selectively for CO_2. Hence, CMK-5 with COOH functionalization is a suitable material for efficient gas separation.

5. Conclusions

Adsorption mechanisms of CO_2, CH_4, N_2 on functionalized CMK-5 arrays were investigated using GCMC simulations. The Langmuir isotherm model was found to fit the adsorption isotherms extremely well. The adsorption behavior was analyzed using adsorption isotherms, local density distribution and the isosteric heat of adsorption of pure gases. It was observed that functionalization affected the adsorption isotherms. More precisely, upon functionalization, the uptake increases for CO_2; however, it slightly decreases for CH_4. On the other hand, negligible enhancement of nitrogen adsorption can be seen for –COOH functionalization. In terms of adsorption capacity, –COOH functionalized CMK-5 was much more favorable than –OH functionalized CMK-5. Moreover, it was observed that the pore diameter plays a major role in the adsorption isotherms for pure gases. For all adsorbates, the excess adsorption isotherm decreases with increasing pore diameter. The effect of inter-tube distance was found to be negligible on the adsorption behavior of flue gases. Inter-tube spacing also affects the excess adsorption of CO_2, CH_4, and N_2. For low pressure, $p \leq 18$ bar, maximum adsorption was observed for $d = 0.25$ nm, followed by $d = 0.5$ nm in the pressure range of $18 < p \leq 30$ bar. However, for $p > 30$ bar, the maximum adsorption was observed at $d = 1.0$ nm. For methane and nitrogen, the maximum uptake was found at $d = 0.25$ nm in the studied pressure range.

The adsorption mechanism was further investigated for equimolar binary mixtures of CO_2–CH_4, CO_2–N_2 and CH_4–N_2. The selectivity of these gases was predicted using IAST theory. For the CO_2–CH_4 binary mixture, the selectivity of CO_2 was highest for the –COOH functionalized CMK-5 system. The selectivity was found to follow the order $S_{CH_4\text{–}N_2} < S_{CO_2\text{–}CH_4} < S_{CO_2\text{–}N_2}$. Considering the twofold higher selectivity of CO_2 over other gases for –COOH functionalized CMK-5 as opposed to bare CMK-5, CMK-5 with COOH functionalization was found to be a suitable adsorbent for efficient gas separation.

Acknowledgements

This study has been supported by the Ministry of Earth Sciences, Govt. of India. The computational facility was provided by HPC, Computer Centre, Indian Institute of Technology Kanpur.

Notes and references

1 H. Kabbour, T. F. Baumann, J. J. H. Satcher, A. Saulnier and C. C. Ahn, *Chem. Mater.*, 2006, **18**, 6085.
2 Z. X. Yang, Y. D. Xia and R. Mokaya, *J. Am. Chem. Soc.*, 2007, **129**, 1673.
3 S. J. Gregg and K. S. W. Sing, *Adsorption, Surface Area and Porosity*, Academic Press, London, 2nd edn, 1982.
4 T. Kyotani, *Carbon*, 2000, **38**, 269.
5 P. A. Heiley, *J. Phys. Chem. Solids*, 1992, **53**, 1333.
6 A. Thess, R. Lee, P. Nikolaev, H. Dai, P. Petit, J. Robert, C. Xu, Y. H. Lee, S. G. Kim, D. T. Colbert, G. E. Scuseria, D. Tomanek, J. E. Fisher and R. E. Smalley, *Science*, 1996, **273**, 483.
7 Q. Song, S. Jiang, T. Hasell, M. Liu, S. Sun, A. K. Cheetham, E. Sivaniah and A. I. Cooper, *Adv. Mater.*, 2016, **28**, 2629–2637.
8 H. Yang and D. Zhao, *J. Mater. Chem.*, 2005, **15**, 1217.

9 R. Ryoo, S. H. Joo and S. Jun, *J. Phys. Chem. B*, 1999, **103**, 7743.
10 A. B. Fuertes and D. M. Nevskaia, *J. Mater. Chem.*, 2003, **13**, 1843.
11 L. A. Rodrigues, M. L. C. P. d. Silva, M. O. Alvarez-Mendes, A. d. R. Coutinho and G. P. Thim, *Chem. Eng. J.*, 2011, **174**, 49–57.
12 H. Tamai, T. Kakii, Y. Hirota, T. Kumamoto and H. Yasuda, *Chem. Mater.*, 1996, **8**, 454.
13 R. J. Littel, G. F. Versteeg and W. P. M. Swaaij, *Chem. Eng. Sci.*, 1991, **46**, 3308–3313.
14 S. Bishnoi and G. T. Rochelle, *Chem. Eng. Sci.*, 2000, **55**, 5531–5543.
15 A. Aroonwilas and A. Veawab, *Ind. Eng. Chem. Res.*, 2004, **43**, 2228–2237.
16 S. Choi, J. H. Drese and C. W. Jones, *ChemSusChem*, 2009, **2**, 796–854.
17 A. Sayari, Y. Belmabkhout and R. Serna-Guerrero, *Chem. Eng. J.*, 2011, **171**, 760–774.
18 G. M. Plaza, S. Garcia, F. Rubiera, J. J. Pis and C. Pevida, *Chem. Eng. J.*, 2010, **163**, 41–47.
19 Q. A. Wang, J. Z. Luo, Z. Y. Zhong and A. Borgna, *Energy Environ. Sci.*, 2011, **4**, 42–55.
20 X. Liu, J. Li, L. Zhou, D. Huang and Y. Zhou, *Chem. Phys. Lett.*, 2005, **415**, 198–201.
21 Y. Sun, X. W. Liu, W. Su, Y. Zhou and L. Zhou, *Appl. Surf. Sci.*, 2007, **253**, 5650–5655.
22 T. L. Chew, A. L. Ahmed and S. Bhatia, *Adv. Colloid Interface Sci.*, 2010, **153**, 43–57.
23 A. R. Millward and O. M. Yaghi, *J. Am. Chem. Soc.*, 2005, **127**, 17998–17999.
24 Q. Yang, C. Zhong and J. F. Chen, *J. Phys. Chem. C*, 2008, **112**, 1562–1569.
25 R. Banerjee, H. Furukawa, D. Britt, C. Kobler, M. O'Keeffe and O. M. Yaghi, *J. Am. Chem. Soc.*, 2009, **131**, 3875–3877.
26 S. R. Caskey, A. G. Wong-Foy and A. J. Matzger, *J. Am. Chem. Soc.*, 2008, **130**, 10870–10871.
27 L. Bastin, P. S. Barcia, E. J. Hurtado, J. A. C. Silva, A. E. Rodrigues and B. Chen, *J. Phys. Chem. C*, 2008, **112**, 1575–1581.
28 B. Liu and B. Smit, *Langmuir*, 2008, **25**, 5918–5926.
29 H. Furukawa and O. M. Yaghi, *J. Am. Chem. Soc.*, 2009, **131**, 8875–8883.
30 M. Cinke, J. Li, C. W. Bauschlicher, A. Ricca and M. Meyyappan, *Chem. Phys. Lett.*, 2003, **376**, 761–766.
31 D. N. Futaba, K. Hata, T. Namai, T. Yamada, K. Mizuno, Y. Hayamizu, M. Yumura and S. Iijima, *J. Phys. Chem. B*, 2006, **110**, 8035–8038.
32 D. N. Futaba, K. Hata, T. Yamada, T. Hiraoka, Y. Hayamizu, Y. Kakudate, O. Tanaike, H. Hatori, M. Yumura and S. Iijima, *Nat. Mater.*, 2006, **5**, 987–994.
33 T. Yamada, T. Namai, K. Hata, D. N. Futaba, K. Mizuno, J. Fan, M. Yudasaka, M. Yumura and S. Iijima, *Nat. Nanotechnol.*, 2006, **1**, 131–136.
34 M. Rahimi, J. K. Singh, D. J. Babu, J. J. Schneider and F. Muller-Plathe, *J. Phys. Chem. C*, 2013, **117**, 13492–13501.
35 W.-Q. Deng, X. Xu and W. Goddard, *Phys. Rev. Lett.*, 2004, **92**, 166103.
36 M. Rahimi, J. K. Singh and F. M. Plathe, *J. Phys. Chem. C*, 2015, **119**, 15232–15239.
37 S. H. Joo, S. J. Choi, I. Oh, J. Kwak, Z. Liu and O. Terasaki, *Nature*, 2001, **412**, 169–172.
38 M. Kruk, M. Jaroniec, T. W. Kim and R. Ryoo, *Chem. Mater.*, 2003, **15**, 2815–2823.
39 T. Kim, M. Kim, Y. Yang, J. Kim, S. Jeong and C. Kim, *Int. J. Hydrogen Energy*, 2015, **40**, 15236–15243.
40 R. J. M. Pellenq, S. Rodts, V. Pasquier, A. Delville and P. Levitz, *Adsorption*, 2000, **6**, 241.
41 B. Coasne, F. R. Hung, R. J. M. Pellenq, F. R. Seperstein and K. E. Gubbins, *Langmuir*, 2006, **22**, 194.
42 R. J.-M. Pellenq and D. Nicholson, *J. Phys. Chem.*, 1994, **98**, 13339.
43 D. W. Brenner, *Phys. Rev. B: Condens. Matter Mater. Phys.*, 1990, **42**, 9458.
44 X. Peng, D. P. Cao and W. C. Wang, *Langmuir*, 2009, **25**, 10863.
45 J. J. Potoff and J. I. Siepmann, *AIChE J.*, 2001, **47**, 1676–1682.
46 M. Kim and J. Chang, *Korean J. Chem. Eng.*, 2015, **32**, 939–949.
47 W. L. Jorgensen, J. M. Briggs and M. L. Conteras, *J. Phys. Chem.*, 1990, **94**, 1683.
48 J. G. Harris and K. H. Yung, *J. Phys. Chem.*, 1995, **99**, 12021–12024.
49 H. A. Lorentz, *Ann. Phys.*, 1881, **12**, 127–136.
50 S. J. Mahdizadeh and S. F. Tayyari, *Theor. Chem. Acc.*, 2011, **128**, 231–240.
51 D. D. Do and H. D. Do, *J. Phys. Chem. B*, 2006, **110**, 7531–17538.
52 Z. Liua, T. Horikawa, D. D. Do and D. Nicholson, *J. Colloid Interface Sci.*, 2012, **368**, 474–487.
53 A. L. Myers and P. A. Monson, *Langmuir*, 2002, **18**, 10261–10273.
54 T. Vuong and P. A. Monson, *Langmuir*, 1996, **12**, 5425–5432.
55 W. Humphrey, A. Dalke and K. Schulten, *J. Mol. Graphics*, 1996, **14**, 33–38.
56 S. K. Jain, R. J.-M. Pellenq, J. Pikunic and K. E. Gubbins, *Langmuir*, 2006, **22**, 9942.
57 S. K. Jain and K. E. Gubbins, *Langmuir*, 2007, **23**, 1123.
58 G. R. Birkett and D. D. Do, *J. Phys. Chem. C*, 2007, **111**, 5735.
59 L. Zhou, X. Liu, J. Li, N. Wang, Z. Wang and Y. Zhou, *Chem. Phys. Lett.*, 2005, **413**, 6–9.
60 X. Peng, D. Cao and W. Wang, *Chem. Eng. Sci.*, 2011, **66**, 2266–2276.
61 L. Huang, L. Zhang, Q. Shao, L. Lu, X. Lu, S. Jiang and W. Shen, *J. Phys. Chem. C*, 2007, **111**, 11912–11920.
62 P. Kowalczyk, S. Furmaniak, P. A. Gauden and A. P. Terzyk, *J. Phys. Chem. C*, 2010, **114**, 21465–21473.
63 M. Rzepka and P. Lamp, *J. Phys. Chem. B*, 1998, **102**, 10894–10898.
64 X. Peng, D. Cao and W. Wang, *J. Phys. Chem. C*, 2008, **112**, 13024–13036.

